

Received 15 August 2023; revised 23 October 2023 and 7 December 2023; accepted 28 December 2023. Date of publication 10 January 2024;
date of current version 22 January 2024. The review of this article was arranged by Associate Editor Mauro Di Nardo.

Digital Object Identifier 10.1109/OJIA.2024.3352134

An Alternative Run-Up Strategy for Salient Pole Wound Field Synchronous Machines

ROBERTO FELICETTI , VINÍCIUS M. DE ALBUQUERQUE , AND URBAN LUNDIN 

Department of Engineering Sciences, Division of Electricity, Uppsala University, 751 21 Uppsala, Sweden

CORRESPONDING AUTHOR: ROBERTO FELICETTI (e-mail: roberto.felicetti@angstrom.uu.se)

(Roberto Felicetti and Vinícius M. de Albuquerque are co-first authors.)

This work did not involve human subjects or animals in its research.

ABSTRACT Salient pole wound field synchronous motors find many industrial applications, thanks to their favorable characteristics: reactive power regulation, stiff mechanical characteristic, and overall outstanding efficiency. Nevertheless, their competitiveness toward the induction motors, especially for medium and small power sizes, depends crucially on their capability to be asynchronously started as well. Regrettably, the asynchronous run-up of a synchronous motor can be sometimes very problematic because of thermal issues, torsional vibrations, and grid voltage disturbances. This article presents an alternative method of starting salient pole wound field synchronous machines by activating the field winding in a special manner, which makes it possible to mitigate the three problems at once. The suggested method is validated through a two-dimensional finite elements simulation and by starting a 60-kVA prototype generator. The requirements for the application of the proposed run-up strategy are critically discussed together with related pros and cons.

INDEX TERMS Asynchronous start, reluctance torque, run-up, salient pole rotor, synchronous motor (SM), torque ripple.

I. INTRODUCTION

Asynchronous motors (AMs) are robust, low maintenance, and are relatively cheap when compared with other types of electric motors [1]. These three features make AMs ideal as industrial prime movers. However, when the high efficiency is a priority, the synchronous motor (SM) can perform better than the asynchronous one [2], [3]. This is the case in many low-speed¹ automotive drives where the permanent magnet synchronous motor helps greatly in saving battery energy [4], [5]. This is also the case of the pumped storage power plants, where the high efficiency of the synchronous machine contributes to the overall round-trip efficiency of the system [6], [7]. Moreover, it does not present the stability risk posed by the double-fed asynchronous generator [8] and is able to provide black start capability [9]. Besides, in those applications, where the considerable reactive power consumption of AMs represents an economic or technical challenge, SMs are

the natural alternative choice. Finally, where constant speed and pace keeping of all involved drives are crucial for a productive process—such as in the paper and steel rolling mill industry—SMs can provide the stiff mechanical characteristic that the applications need. Nevertheless, at the state-of-the-art, units of MW output represent the break even for industrial applications of SMs, where AMs are more attractive for smaller sizes, due to their relative lower cost and maintenance need [10].

The toughest burden of SMs is that they need to be synchronized at the grid frequency in order to work properly and efficiently. The SM run-up through a variable frequency converter is the most effective and efficient way to reach the synchronism. However, the considerable cost of this device makes its use convenient when a variable speed control is strictly required [9]. Therefore, the synchronized asynchronous motors (SAMs) [11] and line-start synchronous motors (LSSMs) [12], [13], [14], [15], [16] have been studied and developed over the past decades, aiming to keep the design and the run-up solutions simple and robust at the same

¹For high-speed automotive drives, the high iron losses produced by the PM could make the induction motor more efficient.

time. Unfortunately, they suffer the same and sometimes even larger problems than the AMs during the start. In fact, the asynchronous LSSMs can be troublesome for at least three main reasons:

- 1) the thermal stress produced in the rotor for long or repeated starts;
- 2) the remarkable ripple that characterizes the starting torque;
- 3) the low steady-state power factor.

The almost adiabatic warming up in the rotor during the start skyrockets the temperature of those conductive parts where the eddy currents are induced (damper bars, solid pole shoes, permanent magnets, etc.) [17], [18]. The related negative consequences of exceptional temperature rise in the rotor can include the mechanical breakdown for fatigue, the magnet total or partial demagnetization, and the accelerated aging or failure of the electric insulation. The characteristics of the load faced during the run-up, the rotor inertia, as well as the length of the starting time are all responsible for the severity of the considered warm-up [18]. Furthermore, the magnetic and electric asymmetries of the rotor, due to the salient poles, the damping bars, and the PMs are the causes of the ripple in the starting torque [19], [20], [21], [22]. The ripple is quite nasty because it is variable in intensity (large at standstill and close to the synchronism) and its frequency changes steadily from twice the grid frequency to zero along the entire run-up process [23]. This fact can easily trigger the vibrational modes of the driving system, which would, in turn, accelerate the wear and tear of the mechanic couplings or produce the failure of mechanical elements in the driving chain. For preventing the overheating of the line-started SM and/or for limiting the driving torque ripple during the startup, some protective devices are needed. They are called either startup protections [18]—when they tackle the thermal issue only—or smooth startup units (SSUs) [24], [25], [26] when they reduce both the current inrush and the torque ripple. These devices increase the specific costs of the SMs drive furtherly and, above all, they reduce the locked rotor torque (LRT) and the pull-up torque (PUT) of the protected motors.

In this article, an asynchronous starting strategy for an salient pole wound field synchronous machine (SPWFSM) is presented that does not produce thermal issues for the rotor at the run-up, provides good LRT and PUT levels, and reduces the torque ripple if compared with an asynchronous line start. It makes use of special arrangements for the excitation system (ES) and the rotor winding that are duly illustrated in Section III. The suggested run-up strategy is tested on a 60-kVA SPWFSM prototype and the experimental results are furtherly validated through a 2-D finite elements method (FEM) transient simulation. The rest of this article is organized as follows. Section II describes a brief recall of the main causes for the torque ripple. Section III presents a multiphase rotor winding concept analyzing its dc and ac behaviors. The experimental setup and the simulation concept are then introduced and explained in Section IV. Next, a run-up of the machine at constant acceleration is both performed and

simulated. The obtained results are reviewed and discussed in Section V. Finally, Section VI concludes this article.

II. CAUSES OF THE TORQUE RIPPLE

The torque in a salient pole synchronous machine during the line start consists of three terms essentially [23]: a useful constant unidirectional component T_{avg} , averaged over the slip period; an unavoidable fast decaying pulsating torque $T_{tran}(t)$, which relates to the transient components of the armature and rotor currents; and an undesired persistent pulsating torque $T_{rip}(t)$, which causes the machine torsional vibrations. The latter component has been intensively investigated [19], [20], [21], [22], [23] finding out that it depends mainly on the following rotor aspects:

- 1) the difference in magnetic permeance between the d - and q -axis (due to the rotor saliencies);
- 2) uneven angular distribution of the rotor *proper* electric circuits (field winding and damper bars) and *de facto* electric circuits (pole shoes and pole cores).

With reference to point 1), when the armature windings provide a magnetization for the motor (e.g., during a direct line start of an SM), the reluctance torque $T_{rel,s}$ depends on the amplitude of the stator current and on the difference between the motor magnetization inductances [27]

$$T_{rel,s} \propto \hat{I}_s^2 (L_{dm} - L_{qm}) \sin 2\gamma. \quad (1)$$

The angle γ in (1) lies between the direction of the d -axis and that of the armature magnetomotive force (MMF). When a rotor current I_{exc} magnetizes the machine instead, a change in the angular rotor position ϑ does not change the value of the rotor magnetizing inductance $L_{m,r}$ essentially. Hence, the reluctance torque $T_{rel,r}$ calculated by means of the magnetic coenergy variation [28] by

$$T_{rel,r} \propto -\frac{\partial L_{m,r}}{\partial \vartheta} I_{exc}^2 \cong 0 \quad (2)$$

becomes negligible.

Equation (2) points to the fact that providing the motor magnetization from the rotor side would help to reduce the reluctance component of the torque ripple during the asynchronous start. This is especially relevant considering that the magnetizing current accounts for 30%÷60% of the rated active current component in large AMs [29]. In large SMs, which have relative wider airgaps than AMs, the proportion between magnetizing and active current at the run-up could become even larger.

With reference to point 2), it is well known that the excitation circuit, the damper bars, and the solid amortisseurs (e.g., the pole shoes and conductive magnets) in SPWFSMs can be conveniently represented by single-phase circuits [30]. They produce their MMFs on the d - and/or q -axis only. Fig. 1 shows the fundamental MMF produced by an ac current at slip frequency, having phase constant φ_0 , that flows either through the field winding or the d -axis damper circuit.

The resulting rotor MMF is the sum of a progressive and a regressive wave $\tilde{\Theta}_{r,1}^+$ and $\tilde{\Theta}_{r,1}^-$, respectively. When an

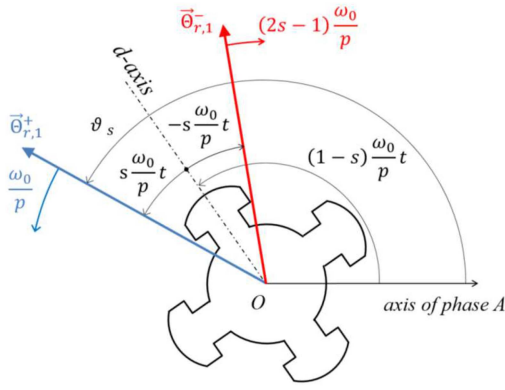


FIGURE 1. Single-phase rotor circuit excited by an ac current at slip frequency produces two counter-rotating MMFs.

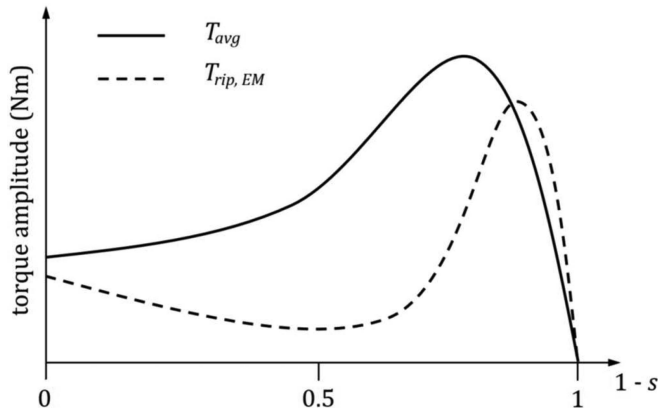


FIGURE 2. Qualitative comparison between the average torque (continuous line) and the ripple torque (dashed line) contributed by a rotor single-phase circuit.

armature-rotating MMF is provided through a direct sequence system of three-phase currents with amplitude \hat{I} and angular frequency ω_0

$$\bar{I}_X = \hat{I}e^{i\omega_0 t}, \bar{I}_Y = \hat{I}e^{i\omega_0 t - \frac{2}{3}\pi}, \bar{I}_Z = \hat{I}e^{i\omega_0 t - \frac{4}{3}\pi} \quad (3)$$

the interaction between the resulting rotating magnetic field and the rotor MMFs establishes the following electromagnetic torque T_{EM} on the rotor

$$T_{EM}(t) = T_{avg} + T_{rip, EM} \sin(2s\omega_0 t + \varphi_0) \quad (4)$$

where the phase constant φ_0 means that the variable component of the torque is not necessarily zero at $t = 0$.

The first term on the right side of (4) is the useful torque T_{avg} . The second term of (4), with amplitude $T_{rip, EM}$, is the contribution of a single-phase rotor circuit to the torque ripple $T_{rip}(t)$. It is due to the interaction between the armature magnetic field and the regressive rotor MMF $\vec{\Theta}_{r,1}^-$, which rotate in the opposite direction.

Fig. 2 shows a comparison between the useful T_{avg} and the undesired $T_{rip, EM}$ in terms of amplitude versus the relative rotor speed [19].

It can be observed that the ripple torque is particularly strong both at the start and close to the synchronism. Its relative intensity depends, among other factors, on the constitution of the rotor. Owen [19] has shown that solid poles in place of laminated ones—especially when the pole tips galvanic connections are not used—can make the amplitude of the ripple torque even larger than the average one that can result in the impossibility to asynchronously start an SPWFSM or to drive it even close to the synchronism. This is because of the solid poles, which, contrarily to other kinds of amortisseurs (e.g., squirrel cage or interconnected grill damper bars), establish a single-phase circuit on the d -axis only, exactly as the field winding does.

Having examined the different contributions to the ripple torque during the asynchronous run-up, previously addressed with points 1) and 2), respectively, it is concluded that:

- 1) magnetizing the machine from the rotor side;
 - 2) making the rotor circuits symmetric so as to form symmetric multiphase windings;
 - 3) adopting laminated poles;
- are all means for reducing the ripple torque.

The implementations of the technical solutions referred to in points 1–3 above are presented in Section III for SPWFSMs. In particular, Section III-A describes a novel rotor arrangement, which is electrically and magnetically symmetric during the asynchronous run-up phase, when it is supplied with ac currents. The same arrangement can excite the SM at synchronism when dc is supplied. Section III-B shows how to connect the armature phases conveniently so as to correspond to the rotor MMF during the asynchronous and synchronous behaviors, respectively. After the derivation of the run-up torque in Section III-C, the driving strategy for the run-up and the test setup is disclosed. The presentation of the time-stepping FEM simulation of the run-up concept is considered in Section III-G and its results are compared with the experimental results in Section V.

III. METHOD

A. MULTIPHASE ROTOR WINDING AND ITS MMF ANALYSIS

In Fig. 3, a special rotor winding arrangement is shown [31], where four phases are formed by connecting the pole winding every four poles so that for $k = 0, 1, 2, \dots$, the poles involved in the m th phase (where $m = 1, 2, 3, 4$) are

$$n_{m,k} = m + 4k. \quad (5)$$

All-phase ends are then joined together to form a common electric reference point. In the end, there are five winding terminals, one for each strand, and one for a common reference O . Fig. 3(a) shows that, when the same dc current enters the odd phases and exits the even ones, a constant excitation field with $2p$ poles is set up. Therefore, the shown field windings are able to provide the excitation field needed by an SPWFSM at synchronism. Fig. 3(b) and (c) are referred to the following

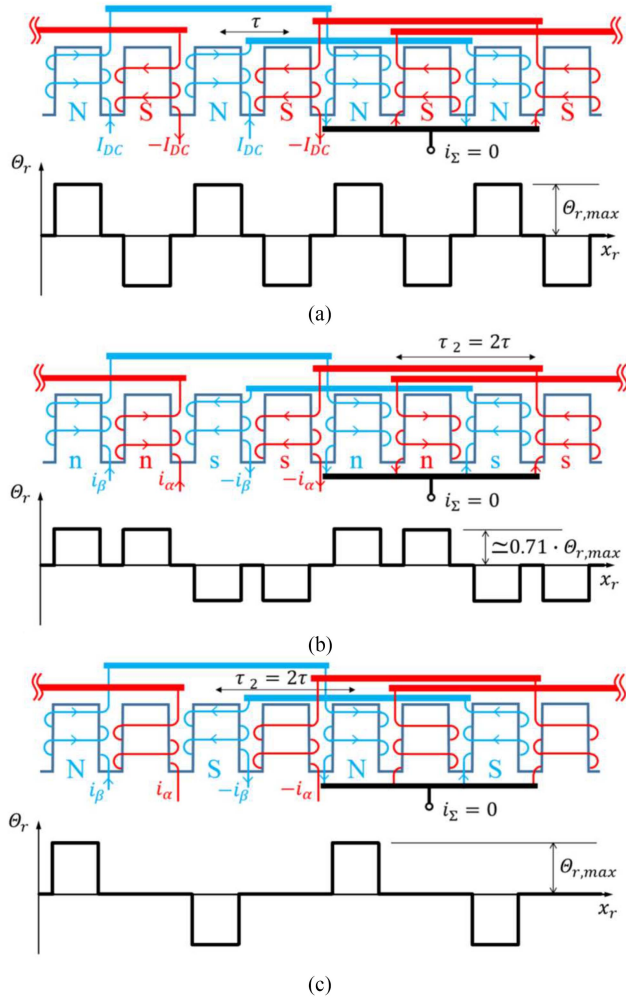


FIGURE 3. Multiphase salient pole rotor windings arrangement capable of producing (a) DC excitation field having $2p$ poles, and (b) and (c) rotating magnetic field having p poles, when supplied by two sinusoidal currents in quadrature. In (b) $i_\alpha = i_\beta$ and in (c) i_β is maximal while $i_\alpha = 0$.

sinusoidal currents in quadrature, having electric angular frequency ω_e

$$i_\alpha = I_f \cos \omega_e t \quad (6)$$

$$i_\beta = I_f \cos \left(\omega_e t - \frac{\pi}{2} \right). \quad (7)$$

The current i_β enters the first phase and exits the third one, whereas i_α enters the second phase and exits the fourth one.

After one-eighth of the electric period, when $i_\alpha = i_\beta \cong 0.71 I_f$, a magnetic field is set by the rotor, which shows only p poles. As a result of this, in Fig. 3(b), the new pole pitch τ_2 is twice the original pole pitch τ of the SM. In Fig. 3(c), after one-fourth of the electric period, when $i_\alpha = 0$ and $i_\beta = I_f$, the magnetic field of the rotor still shows p poles. However, it has moved half a pole leftward with respect to the previous instant. Having displaced of about π/p radians in $T/8$ seconds, the magnetic field produced by (6) and (7) has a positive mechanical angular speed (referred to as the rotor)

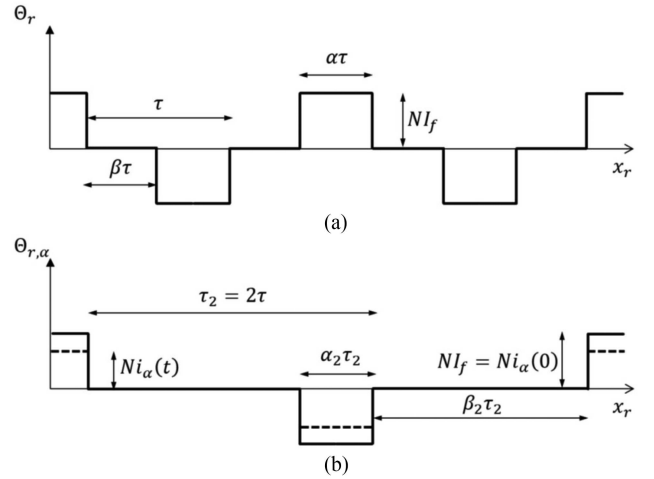


FIGURE 4. Simplified rotor MMF profile for a salient pole rotor having pole coverage α and N turns per coil. (a) When i_α and $-i_\beta$ are dc currents equal to I_f . (b) When i_α is a sinusoidal current with amplitudes I_f and $i_\beta = 0$.

equal to

$$\Omega_r = \frac{2}{p} \omega_e. \quad (8)$$

Equation (8) proves that the field windings arrangement, as represented in Fig. 3, is able to provide a rotating magnetic field as well, the angular speed of which is related to the frequency of the sinusoidal rotor currents i_α and i_β . Fig. 4(a) represents the simplified profile of the rotor MMF Θ_r along the rotor perimeter. The rotor has pole coverage α , N turns per coil, p pole pairs, and a dc current supply mode according to Fig. 3(a).

The harmonic expansion of Θ_r is a function of the sole mechanical rotor angle ϑ_r and includes odd-order harmonics only

$$\Theta_r(\vartheta_r) = \frac{4}{\pi} NI_e \sum_0^{\infty} a_{2k+1} \cos[(2k+1)p\vartheta_r]. \quad (9)$$

The amplitudes of the harmonics depend on the pole coverage through the following coefficients:

$$a_{2k+1} = \frac{1}{2k+1} \cos \left[(2k+1)(1-\alpha) \frac{\pi}{2} \right]. \quad (10)$$

Fig. 4(b) shows the simplified MMF rotor profile in the same rotor arrangement, where the sole current (6) flows. The profile is that of a standing wave showing p rectangular pulses, the amplitude of which varies in time proportionally to $i_\alpha(t)$. The Fourier expansion of a phase MMF in the rotor can be easily derived from (9), having made the needed adjustments

$$\Theta_{r,\alpha}(\vartheta_r, t) = \frac{4}{\pi} Ni_\alpha(t) \sum_0^{\infty} a_{2,2k+1} \cos \left[(2k+1) \frac{p}{2} \vartheta_r \right] \quad (11)$$

Equation (11) is a function of both rotor angle ϑ_r and time t . The harmonics' amplitudes in (11) are proportional to

$$a_{2, 2k+1} = \frac{1}{2k+1} \cos \left[(2k+1) \frac{2-\alpha}{2} \cdot \frac{\pi}{2} \right] \quad (12)$$

where the first subscript "2" points to the fact that these coefficients are related to the two current modes of Fig. 3(b) and (c). The MMF produced by the sole (7) can be obtained per analogy from (11) by

$$\Theta_{r,\beta}(\vartheta_r, t) = \frac{4}{\pi} N i_\beta \sum_0^\infty a_{2,2k+1} \cos \left[(2k+1) \left(\frac{p}{2} \vartheta_r - \frac{\pi}{2} \right) \right] \quad (13)$$

At this point, the rotor MMF $\Theta(\vartheta_r, t)$, established by two 90° displaced sinusoidal currents, can be obtained by adding (11) and (13) and using some trigonometry. The following result is yielded:

$$\begin{aligned} \Theta(\vartheta_r, t) = & \frac{4}{\pi} N I_e \sum_0^\infty a_{2,4k+1} \cos \left[(4k+1) \frac{p}{2} \vartheta_r \mp \omega_e t \right] \\ & + \frac{4}{\pi} N I_e \sum_0^\infty a_{2,4k+3} \cos \left[(4k+3) \frac{p}{2} \vartheta_r \pm \omega_e t \right]. \end{aligned} \quad (14)$$

In (14), the upper signs in the cosine argument are used when i_α leads on i_β as in (6) and (7). Sticking to this assumption, the rotor MMF (14) is the superposition of two groups of odd-order rotating waves: the group of the progressive MMF waves, associated with the orders 1st, 5th, 7th, ..., $(4k+1)$ th and having mechanical speed with respect to the rotor

$$\Omega_{r,4k+1} = \frac{1}{4k+1} \Omega_r \quad (15)$$

and the group of the regressive MMF waves, associated with the orders 3rd, 7th, 11th, ..., $(4k+3)$ th, which have mechanical speed with respect to the rotor

$$\Omega_{r,4k+3} = -\frac{1}{4k+3} \Omega_r. \quad (16)$$

As soon as i_α lags on i_β , the two groups of harmonics swap their roles and the signs of (15) and (16) must be changed accordingly.

Finally, Fig. 5 shows the relative weights of each single harmonic with respect to the fundamental of the MMF of Fig. 4(a), which is the useful one for the SM at synchronism. The weights are given in function of the rotor pole coverage α , for both the steady MMF with $2p$ poles (upper subfigure) and rotating MMF with p poles (lower subfigure). The assumption underlying the two behaviors, as compared in Fig. 4(a), is that the dc current of the synchronous MMF equals the amplitude of the phase currents i_α and i_β of the rotating MMF.

In the same figure, it can be observed that, in the usual range of the pole coverage ($0.65 \div 0.80$), the amplitude of the fundamental of the rotating MMF is about 55%÷60% of the fundamental of the steady MMF. Moreover, the third harmonics of the stationary MMF, which can knowingly be canceled

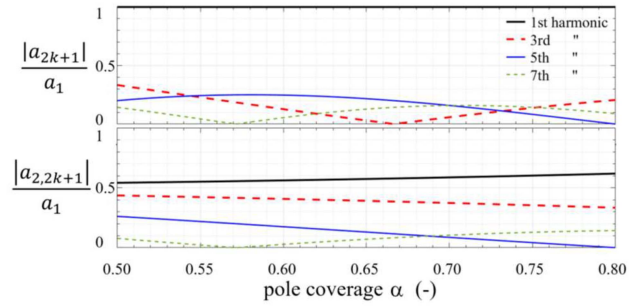


FIGURE 5. Relative amplitudes of the first four nontrivial rotor MMF harmonics, for a stationary MMF (upper plots) and for a rotating one (lower plots), produced by dc and ac currents, respectively, having the same maximal intensity.

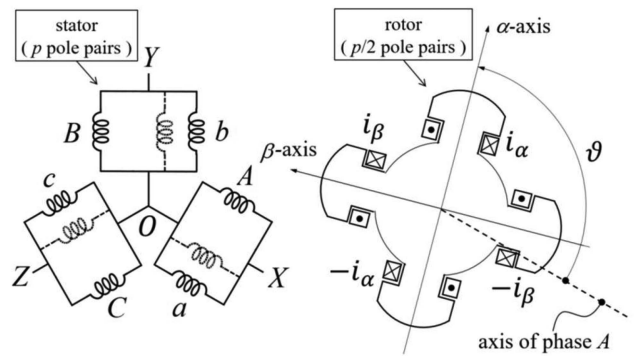


FIGURE 6. According to the proposed rotor winding arrangement, the rotating MMF produced by the ac current supply does not match the number of poles of the armature.

through an appropriate choice of the pole coverage, amounts to circa 40% in the rotating MMF. This poses a problem for the exploitation of the rotating MMF during the run-up. In fact, the third harmonic would act against the accelerating work of the fundamental one, in the same way an external load does. Therefore, this crucial problem is addressed and solved next by considering the armature windings.

B. STATOR WINDINGS ARRANGEMENT

The idea of ac magnetizing the SM from the rotor side during the asynchronous run-up has the advantage of establishing a magnetic and electric symmetry in the rotor, as the right side of Fig. 6 shows.

The rotor presents the same permeance on the d - and q -axis and has identical electric circuits working on them. However, the rotating excitation produced by ac currents in the rotor [see Fig. 3(b) and (c)] shows only p poles, whereas the SM armature is designed for $2p$ poles.

A solution for this "pole mismatch" is possible when the armature presents at least two current paths in parallel for each phase ($c > 1$) [31], the terminals of which can be accessed separately and conveniently connected through toggle switches. Fig. 7 shows a four-pole ($p = 2$) SPWFSM with $c = 2$ parallel

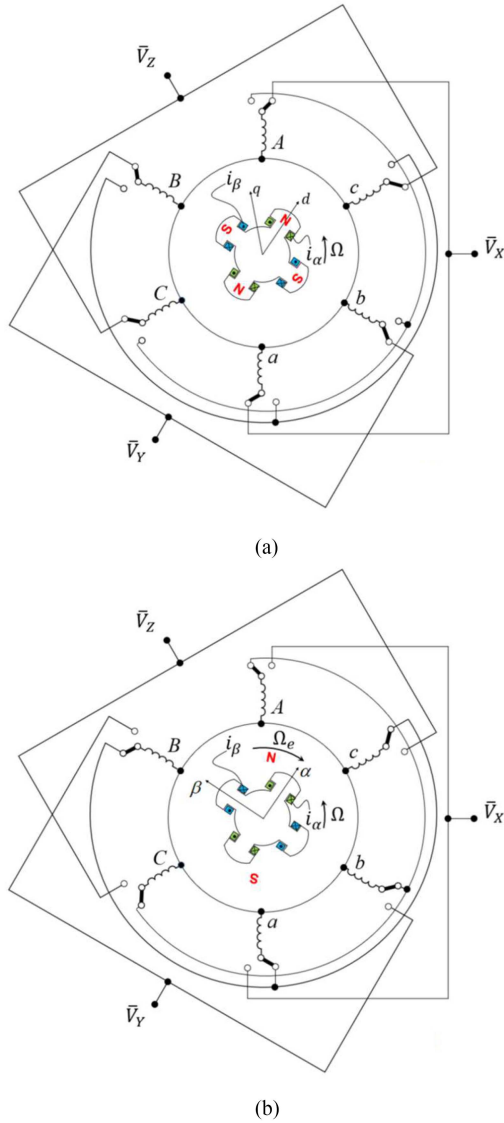


FIGURE 7. Armature phase connections. (a) Synchronous behavior with dc rotor excitation. (b) Asynchronous behavior with ac rotor excitation.

paths per armature phase, which includes the special rotor arrangement, as presented in Section III-A.

In order to find out how to conveniently connect the armature phase during the dc and ac rotor excitation, in the continuation, the electromotive forces (EMFs) of the machine phases are derived from the magnetic linkage fluxes.

In Fig. 7(a) and (b), the generic harmonic of the magnetizing flux linked with phase A can be expressed by means of

$$\Psi_{2m+1,A} = \hat{\Psi}_{2k+1} \cos [p(\Omega_e + \Omega)t] = \text{Re} [\bar{\Psi}_{2m+1,A}] \quad (17)$$

where Ω_e is the angular speed of the rotor magnetic field with respect to the rotor and Ω is the rotor angular speed.

Once the vector $X \equiv [A, B, C, a, b, c]$ is defined, the position $k_x \in [1, 2, 3, 4, 5, 6]$ of the element x belonging to X

	1 st harmonic	3 rd harmonic
DC-excitation		
AC-excitation		

FIGURE 8. First and third harmonics of the EMFs induced in the armature phases in Fig. 7 by a dc excitation (rotor spinning CCW) and by a retrograde ac excitation (rotor spinning CCW), respectively.

is

$$k_x \equiv \text{pos}(x \in X). \quad (18)$$

Therefore, the linked flux for the generic phase x can be generalized as

$$\bar{\Psi}_{2m+1,x} = \bar{\Psi}_{2m+1,A} e^{\mp i(2m+1)(k_x-1)p\frac{\pi}{3}} \quad (19)$$

where the minus sign is taken when $(\Omega_e + \Omega) > 0$ counter-clock-wise (CCW).

The generic harmonic for the EMF of phase A can be derived from (19) by means of the electromagnetic induction law, i.e.,

$$\bar{E}_{2m+1,A} = -i(2m+1)p(\Omega_e + \Omega)\bar{\Psi}_{2k+1,A}. \quad (20)$$

The analogous EMF for the generic phase x is then

$$\bar{E}_{2m+1,x} = \bar{E}_{2k+1,A} e^{\mp i(2m+1)(k_x-1)p\frac{\pi}{3}}. \quad (21)$$

Considering the dc excitation mode at synchronism [see Fig. 7(a)], where $p = 2$ and $\Omega_e = 0$ with $\Omega > 0$, the fundamental harmonic for the phase EMFs becomes

$$\bar{E}_{1x}^{\text{DC}} = \bar{E}_{1A}^{\text{DC}} e^{-i(k_x-1)2\frac{\pi}{3}}. \quad (22)$$

For $x = A, B, \dots, c$, (22) produces the two symmetric direct sequences of voltage in Fig. 8, top-left corner. These allow the toggle-switch positions of Fig. 7(a), which pose the homologous phases (Aa , Bb , and Cc) in parallel during the SM synchronous behavior.

Under the same conditions, considering the third harmonics in (21), the following homopolar EMFs are yielded:

$$\bar{E}_{3x}^{\text{DC}} = \bar{E}_{3A}^{\text{DC}} e^{-i3(k_x-1)2\frac{\pi}{3}}. \quad (23)$$

For $x = A, B, \dots, c$, (22) produces the phasors of Fig. 8, top-right corner. These EMFs are not of concern for the circulation of homopolar currents since the phase windings are y-connected without a neutral line.

Considering now the ac excitation mode for the asynchronous behavior of the SM [see Fig. 7(b)], where $p = 1$ and

$\Omega_e + \Omega = s\Omega_e < 0$ clock-wise (CW) with $\Omega > 0$ (CCW), the fundamental harmonics of the EMFs become

$$\bar{E}_{1x}^{AC} = \bar{E}_{1A}^{AC} e^{+i(k_x-1)\frac{\pi}{3}}. \quad (24)$$

For $x = A, B, \dots, c$, (24) gives the phasors of Fig. 8, bottom-left corner, where two direct three-phase systems of voltages, AbC and aBc , respectively, are represented.

Under the same conditions, the third harmonics of the phase EMFs from (21) are

$$\bar{E}_{3x}^{AC} = \bar{E}_{3A}^{AC} e^{+i3(k_x-1)\frac{\pi}{3}}. \quad (25)$$

For $x = A, B, \dots, c$, (25) identifies the phasors of Fig. 8, bottom-right corner. In this case, the homologous phases, if accidentally connected, would produce third-harmonic circulation currents. However, the toggle-switch positions in Fig. 7(b) prevent such currents to circulate during the SM asynchronous behavior.

C. TORQUE GENERATION FOR THE RUN-UP

During the asynchronous behavior $\omega_e = \Omega_e$ since $p = 1$. Once the phases of each three-phase direct voltage sequence (namely AbC and aBc) are separately closed in a short circuit [see Fig. 7(b)], a double three-phase direct sequence of armature currents is established, so that, analogously to (24)

$$\bar{I}_{1x}^{AC} = \bar{I}_{1A}^{AC} e^{+i(k_x-1)\frac{\pi}{3}}. \quad (26)$$

Considering the voltage balance in one armature phase path having a magnetizing inductance L_{ms} , stray inductance $L_{\sigma s}$, and resistance R_s , the KVL application yields

$$\bar{E}_{1x}^{AC} = -(R_s + is\omega_e L_{\sigma s}) \bar{I}_{1x}^{AC} - \frac{1}{2} is\omega_e \sum_{x,y} M_{xy} \bar{I}_{1y}^{AC}. \quad (27)$$

Since the mutual inductance M_{xy} between the phases x and y is equal to

$$M_{xy} = L_{ms} \cos \left(\text{mod}(k_x - k_y, 6) \frac{\pi}{3} \right) \quad (28)$$

by substituting (28) and (26) in (27), the latter transforms into

$$\bar{E}_{1\mu}^{AC} = \bar{E}_{1x}^{AC} + is\omega_e (3L_{ms}) \bar{I}_{1x}^{AC} = -(R_s + is\omega_e L_{\sigma s}) \bar{I}_{1x}^{AC}. \quad (29)$$

The magnetizing EMF $\bar{E}_{1\mu}^{AC}$, namely

$$\bar{E}_{1\mu}^{AC} = -jL_{\sigma s} s\omega_e \bar{\Psi}_{1,\mu} \quad (30)$$

depends on the magnetizing flux linkage $\bar{\Psi}_{1,\mu}$, which includes the reaction magnetic linkage $-(3L_{ms}) \bar{I}_{1x}^{AC}$ too.

The electromagnetic torque applied to the stator T_{EM}^s can be derived from the active power provided to the six armature phases by

$$T_{EM}^s = \frac{6 \operatorname{Re} \left[\frac{1}{2} \bar{E}_{1\mu}^{AC} \cdot (\bar{I}_{1x}^{AC})^* \right]}{s\omega_e} \quad (31)$$

where $s\omega_e$ is the mechanical angular frequency since $p = 1$.

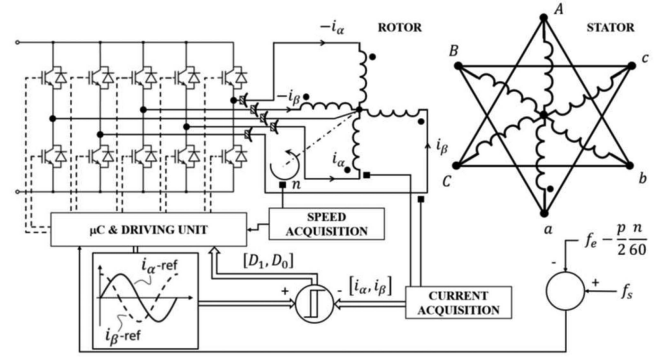


FIGURE 9. Driving arrangement during the startup.

Formulating \bar{I}_{1x}^{AC} in function of $\bar{E}_{1\mu}^{AC}$ from (29), the expression for the torque (31) becomes in the end

$$T_{EM}^s = -6s\omega_e R_s \frac{(\Psi_{1\mu}^{rms})^2}{R_s^2 + (s\omega_e L_{\sigma s})^2}. \quad (32)$$

According to the third law of dynamics, the rotor reacts to (32) with an opposite torque. Hence, it demonstrated that the electromagnetic (EM) torque performs a mechanical work on the rotor in the same sense as the rotor angular speed. This lets us conclude that the asynchronous arrangement, as shown in Fig. 7(b), can definitely work as a motor.

D. DRIVING STRATEGY

During the synchronous behavior of the SPWFSM, the several paths of the armature phases are connected in the way, as shown in Figs. 6 and 7(a). During the proposed alternative asynchronous run-up, the same paths are connected in a short circuit according to Figs. 7(b) and 9 and they play the role of the secondary circuit. The primary circuit is made of the special multiphase rotor winding, as presented in Fig. 3. Since the primary circuit is a rotating one and has five terminals, it is supplied by a five-leg inverter through five sliding contacts.

Contrary to a traditional asynchronous machine, the present one has a rotating primary circuit. A simple change of reference from the stator to the rotor makes it easy to define the motor slip

$$s = \frac{\Omega_{\text{field}} - \Omega_{\text{sec}}}{\Omega_{\text{field}}} = \frac{\omega_e - \frac{p}{2}\Omega}{\omega_e} \quad (33)$$

where Ω_{sec} , Ω_{field} , and Ω are the mechanical angular speeds of the secondary winding (armature), of the rotating magnetic field, and of the rotor, respectively. The numerator of (33) represents the frequency of the induced currents in the armature. By keeping this frequency so low that the armature stray reactance becomes negligible in comparison with the armature resistance, the stator MMF lies almost in quadrature to the rotor magnetizing flux. This ensures knowingly the best condition for the torque generation because the induced armature reaction does not weaken its source. To achieve this

condition, the controlled frequency of the rotor phase currents i_α and i_β must increase together with the rotor speed during the run-up.

In Fig. 9, the microcontroller (μC) generates the reference currents $i_{\alpha\text{-ref}}$ and $i_{\beta\text{-ref}}$ of given frequency f_e , which are reproduced in the rotor phases through a two-point (bang-bang) control strategy. The μC measures the rotor speed n by sensing the rotor position through an incremental encoder mounted on the machine shaft. At a standstill, the excitation frequency equals the desired stator current frequency f_s . As soon as the rotor accelerates under the effect of the generated torque, the actual frequency of the currents induced in the armature phases decreases according to (33). The excitation frequency f_e is kept constant as long as

$$f_s - \left(f_e - p \frac{n}{120}\right) < \Delta f. \quad (34)$$

Otherwise, it is increased stepwise of $\Delta f \ll f_s$ in order to fulfill condition (34) permanently. In this way, the frequency of the induced stator currents can vary very little between f_s and $f_s - \Delta f$, all over the run-up process. Finally, in order to keep the accelerating torque constant while the rotor speed increases, the intensity of excitation flux must not change that can be easily achieved by maintaining the rotor currents amplitude constant, even though their frequency f_e keeps increasing. The bang-bang control performs the rotor currents shaping around the reference currents in Fig. 9. To that end, the dc-link voltage must always be larger than the rotor back EMF to have enough control voltage left for providing the needed current dynamic. Once the desired rotor magnetizing flux linkage $\hat{\Psi}_{\mu r}$ and the maximal current control effort for the hysteresis control are set, the excitation frequency ω_e decides the needed level of the dc-link voltage, according to

$$V_{DC} - \omega_e \hat{\Psi}_{\mu r} > L_{\sigma r} \left| \frac{di_\alpha}{dt} \right|_{\max}. \quad (35)$$

The left side of (35) is the minimal control voltage available at the control frequency ω_e , whereas the right one represents the maximal instantaneous voltage drop on the transient rotor stray inductance $L_{\sigma r}$ at the highest rotor current slope. The combination of (33) and (35) shows that, given the current dynamic, the dc-link voltage, and the magnetizing flux linkage, the higher the rotor speed, the smaller the control voltage available for controlling the rotor currents.

E. SYNCHRONIZATION PROCESS

In principle, having enough dc-link voltage available, it is possible to accelerate an SM, with inertial time constant H , up to a hypersynchronous speed Ω_{hyp} through the conceived starting strategy. At that point, the rotor gets de-excited and the short-circuited stator phases of Fig. 8, at no current, are reconnected back in parallel with their homologs. During this operation, the rotor slows down reaching the synchronous speed Ω_{syn} after

$$\Delta t_{\min} \geq \left(\frac{\Omega_{\text{hyp}}}{\Omega_{\text{syn}}} - 1 \right) 2H \quad (36)$$

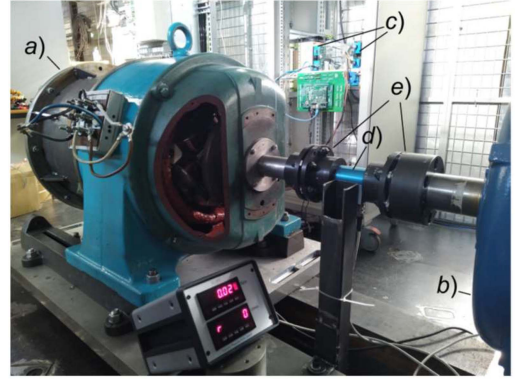


FIGURE 10. Test setup. (a) Driving motor with short-circuited armature phases (A-B-C and a-b-c). (b) Driven machine (additional inertia). (c) 2×200 A H-bridge inverters. (d) Contactless torque sensor. (e) Mechanical joints.

at the earliest, the load torque does not exceed the nominal one. For example, an over-run of the synchronous speed of about 10% would make a lapse of time available larger than 20% of the inertial time constant H . That lapse would be useful for

- 1) switching the armature phases back to the configuration in Fig. 7(a);
- 2) setting up a dc rotor MMF excitation, as shown in Fig. 3(a).

At that point, when the synchronous speed is reached, as soon as the conditions for the EMFs amplitude and phase are achieved, the SPWFSM can be finally connected to the grid.

F. TEST SETUP

In order to demonstrate the run-up of an SPWFSM by means of the suggested concept, a test setup has been built. In Fig. 10, a four-pole, 400 V, 50 Hz, 60 kVA SPWFSM is coupled to a coaxial induction machine through a contactless torque sensor and two mechanical joints. The induction machine is not supplied and has the only function of providing additional inertia to the rotor. With $J_{r,s}$ and $J_{r,i}$ being the rotor moment of inertia of the synchronous and induction machine, respectively, given the torque T_{meas} measured by the torque sensor, the net mechanical torque T accelerating the rotating masses can be indirectly derived by

$$T \cong T_{\text{meas}} \left(1 + \frac{J_{r,s}}{J_{r,i}} \right). \quad (37)$$

Since the dc voltage source available for the test could provide only 170 V of the 410 V needed for the inverter dc link at synchronism, it has been possible to accelerate the rotor at constant torque up to 510 r/min only. Hence, being the test focused mainly on the asynchronous run-up phase rather than on the synchronism, the rotor circuits' connections have been conveniently modified, as shown in Fig. 11, so to have a simplified two-phase system.

This move makes it possible to use only four legs of the inverter (one H-bridge for each phase).

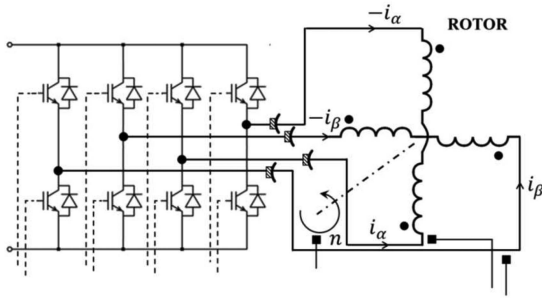


FIGURE 11. Rotor-inverter four-wire connections for demonstrating the run-up only (no synchronism).

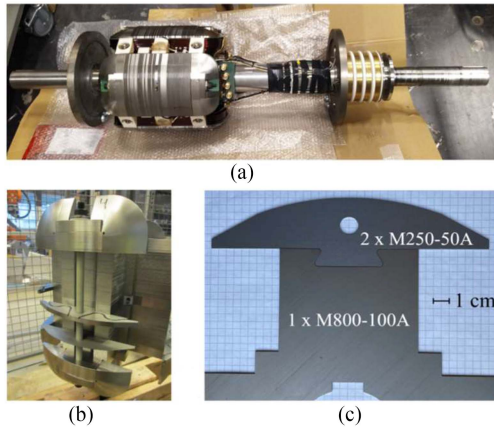


FIGURE 12. Salient pole damperless rotor with a two-phase winding. (a) Assembly. (b) Laminated magnetic circuit. (c) Particular of the pole-shoe/pole-core joint.

In Fig. 12(a), the adopted rotor of the SPWFSM shows only four slips' rings according to the final arrangement of the driving circuit for the test, as already presented in Fig. 11.

In order to prevent the impairment of the variable magnetization flux caused by the eddy currents, the entire magnetic circuit of the rotor is fully laminated [see Fig. 12(b)]. While structural considerations suggest to use a thick lamination for the rim and the pole core, the presence of highly frequent teeth harmonics (stator slots $Q = 72$) requires a thinner lamination for the pole shoes [see Fig. 12(c)]. The needed excitation frequency at synchronism is slightly higher than 25 Hz for $p = 1$. Nongrain-oriented Si electrical steel qualities, such as the ones shown in Fig. 12(c), have $\rho = 400 \text{ n}\Omega\cdot\text{m}$ and $\mu_{r,\max} = 4000$. They experience a minimal penetration depth $\delta = 1 \text{ mm}$ at 25 Hz, which justifies the adoption of M800-100 as the thickest lamination in the rotor design. Finally, the long bolts, that pass through the pole shoes' holes and press the lamination stack together [see Fig. 12(b)], are electrically insulated from the rotor frame by means of glass-fiber/epoxide-wax cylindric cladding and polyamide washers.

G. FIELD-TO-CIRCUIT COUPLED TRANSIENT SIMULATION

The transient simulation of the proposed run-up strategy is performed through an ABB Group internally developed FEM-analysis program called ace. The magnetic field problem is

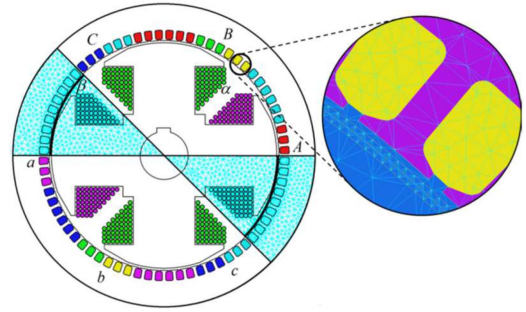


FIGURE 13. Two-dimensional drawing for the FEM analysis coupled with the circuital equations.

based on a 2-D axial cross section of the machine visible in Fig. 13. While the field equations are discretized in the investigated domain, the parameters of the winding coil ends (c.e.), as well as the windings' resistances, have been included in the algorithm through the following circuital equations:

KVL—rotor

$$u_\alpha = e_\alpha + R_r i_\alpha + L_{\sigma r}^{\text{c.e.}} \frac{di_\alpha}{dt} \quad (38)$$

$$u_\beta = e_\beta + R_r i_\beta + L_{\sigma r}^{\text{c.e.}} \frac{di_\beta}{dt}. \quad (39)$$

KVL—for stator phases A, b, and C

$$e_A + R_s i_A + L_{\sigma s}^{\text{c.e.}} \frac{di_A}{dt} = e_b + R_s i_b + L_{\sigma s}^{\text{c.e.}} \frac{di_b}{dt} \quad (40)$$

$$e_b - R_s i_b + L_{\sigma s}^{\text{c.e.}} \frac{di_b}{dt} = e_C + R_s i_C + L_{\sigma s}^{\text{c.e.}} \frac{di_C}{dt}. \quad (41)$$

KVL—for stator phases a, B, and c

$$e_a + R_s i_a + L_{\sigma s}^{\text{c.e.}} \frac{di_a}{dt} = e_B + R_s i_B + L_{\sigma s}^{\text{c.e.}} \frac{di_B}{dt} \quad (42)$$

$$e_B + R_s i_B + L_{\sigma s}^{\text{c.e.}} \frac{di_B}{dt} = e_c + R_s i_c + L_{\sigma s}^{\text{c.e.}} \frac{di_c}{dt}. \quad (43)$$

KCL—for stator phases A-b-C and a-B-c

$$i_A + i_b + i_C = 0 \quad (44)$$

$$i_a + i_B + i_c = 0. \quad (45)$$

Two sinusoidal currents i_α and i_β of constant amplitude, variable frequency, and in quadrature, as shown in Fig. 9, are forced into the rotor phases. Since the armature phases are short circuited according to Fig. 7(b), their currents are the result of their EM interaction with the rotor MMF. The EMFs in (38)–(43) are determined through the postprocessing of the FEM vector potential A_z , by

$$e_x = \frac{l_a}{S} \sum_{i=1}^{n_t} \left(\int_{S_i^+} A_z^+(x, y) dx dy - \int_{S_i^-} A_z^-(x, y) dx dy \right) \quad (46)$$

where l_a is the machine's active axial length, n_t is the number of turns in series per phase, and S_i^+/S_i^- is the cross sections of the conventionally positive and negative active sides of a

turn, respectively. Equations (21)–(45) and (46) set the *field-to-circuit-problem*. For completing the coupling between the field problem and differential problem, the following mechanical differential equations are required:

$$T_{EM} - T_{res} = (J_{r,s} + J_{r,i}) \frac{d\Omega}{dt} \quad (47)$$

and

$$\Omega = \frac{d\vartheta}{dt}. \quad (48)$$

The variable T_{res} summarizes the torque load and the mechanical resistances, while Ω and ϑ are the angular speed and position of the rotor, respectively.

The electromagnetic torque T_{EM} is also obtained by post-processing the vector potential A_z [32] by

$$T_{EM} = \oint_{S_{cyl}} \vec{r} \times \sigma \cdot \hat{n} dS \quad (49)$$

where S_{cyl} is a cylindrical axial domain placed in the motor airgap and $\sigma(A_z)$ is the Maxwell magnetic stress tensor defined as

$$\sigma(A_z) = \begin{bmatrix} \left(\frac{\partial A_z}{\partial y}\right)^2 - \frac{1}{2} \left(\frac{\partial A_z}{\partial x}\right)^2 & -\frac{\partial A_z}{\partial y} \frac{\partial A_z}{\partial x} \\ -\frac{\partial A_z}{\partial x} \frac{\partial A_z}{\partial y} & \left(\frac{\partial A_z}{\partial x}\right)^2 - \frac{1}{2} \left(\frac{\partial A_z}{\partial y}\right)^2 \end{bmatrix}. \quad (50)$$

The vector field A_z is solved by a classic *FEM time-stepping* algorithm [33]. For the run-up simulation, the only independent variable is the amplitude of the rotor currents. In fact, once the Maxwell stress tensor is determined from the FEM results, the Maxwell torque (49) can be numerically calculated. At that point, the rotor speed can be updated instant by instant by integrating the mechanical differential (47) and (48). The used finite-element mesh can be seen in Fig. 13. It contains about 33 000 triangles. The meshing is the finest in the airgap where the surface integral for the EM torque (49) must be performed.

Finally, the ferromagnetic portions of the machine magnetic circuit, made of laminated electrosteel, are modeled by nonlinear cubic splines, which interpolate their magnetization curves. Table 1 lists the machine parameters used for the transient simulation.

IV. RESULTS

The following pictures give a comparison between the experimental and the simulation data for the same run-up test.

In Fig. 14, the excitation frequency starts from 2.5 Hz at the rotor standstill and keeps constant for a while. As soon as the growing rotor speed makes the armature current frequency lower than $f_s = 2$ Hz, the excitation frequency is increased stepwise of $\Delta f = 0.5$ Hz. The linear increase of the rotor speed suggests an underlying constant rotor acceleration. The excitation frequency is increased during the acceleration process, according to (34).

TABLE 1. Steady-State Machine Parameters

Name	Description	Value
r_r	rotor radius	187.5 mm
l_a	machine axial active length	187 mm
δ_{min}	minimal airgap	3.1 mm
δ_{tip}	maximal airgap	5.7 mm
α_{min}	pole coverage (min. airgap)	0.42
α_{tt}	pole coverage (tip-to-tip)	0.73
n	conductors per slot	9
Q	slot number	72
N	number of turns per pole	49
R_r	rotor phase resistance	38 mΩ
R_s	armature phase resistance	300 mΩ
$L_{sr}^{c.e.}$	c.e. stray inductance (rot.)	0.63 mH
$L_{ss}^{c.e.}$	c.e. stray inductance (stat.)	1.80 mH

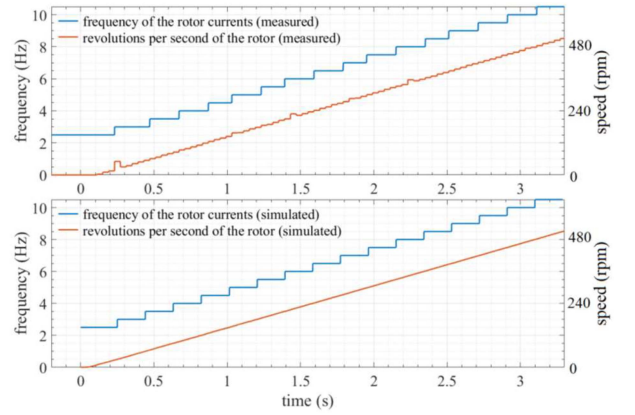


FIGURE 14. Controlled excitation frequency (blue plot) and rotor speed (red plot) during the run-up test and simulation.

The sinusoidal rotor currents, producing a CW rotating excitation field, are presented in Fig. 15. The upper plot reproduces the actual currents, continuously adjusted around their respective sinusoidal references by the bang–bang control (± 2 A as hysteresis window). The frequency control strategy, as represented in Fig. 14, forces the slip frequency between very close limits during the run-up ($2 \leq f_s \leq 2.5$). Hence, the armature currents in the short-circuited phases A, b, and C (see Fig. 16) show an almost constant frequency. The current ripple with variable frequency, more evident in the simulation plot, depends on the rotor saliencies facing the armature phase electric axis four times per revolution.

Finally, Fig. 17 shows the driving torque produced by the proposed run-up strategy.

The upper plot is an indirect measurement of the acceleration torque by means of (37). It shows an average constant value, which is responsible for the constant rotor acceleration. If compared with the simulated EM torque, they differ for the ripple components at higher frequency mainly. Since the simulated torque correctly reproduces an increasing torque ripple frequency ($2ps\omega_e$) at increasing excitation frequency,

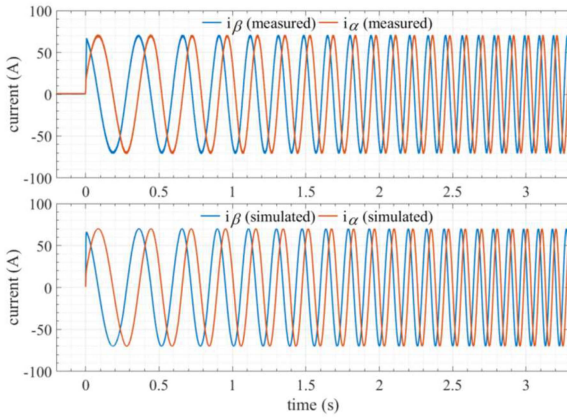


FIGURE 15. Controlled sinusoidal rotor currents. The current i_β is leading on i_α and in phase quadrature to it.

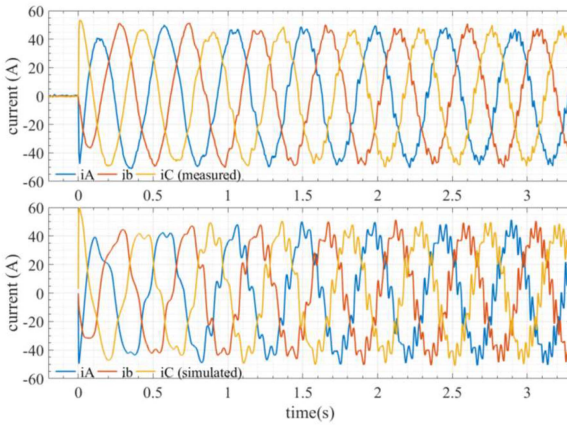


FIGURE 16. Armature currents for the phases A, b, and C. The currents in phases a, B, and c are omitted because they are trivially the opposite of the currents in the homologous phases.

the problem seems to be on the measured torque. This could depend either on the damping and filtering effect of the mechanical elastic joints and/or of the data acquisition chain in the torque sensor.

V. DISCUSSION

In [19], [20], and [23], it is shown how the amplitude of the torque ripple can overcome the average accelerating torque during the traditional line start of an SPWFSM. In particular, that happens close to the synchronism, when the torque component at twice the slip frequency can approach and cross potential natural frequencies of the entire driving chain. On the contrary, Fig. 17 shows that the proposed startup strategy keeps the amplitude of the torque ripple below 30% of its average value, all over the acceleration process. In addition, the torque ripple frequency increases together with the rotor speed instead of decreasing. This is due to the unavoidable presence of the reluctance torque produced by the armature currents. By observing Fig. 18, it is possible to recognize that, given the asynchronous behavior and the magnetizing flux in

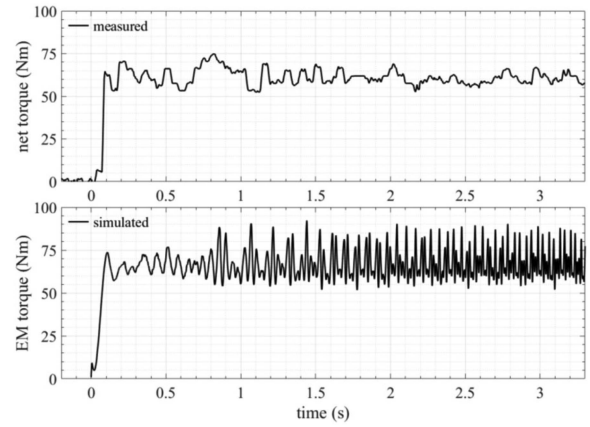


FIGURE 17. Measured net mechanical torque accelerating the rotor (upper plot) and simulated EM torque produced by the driving strategy (lower plot).

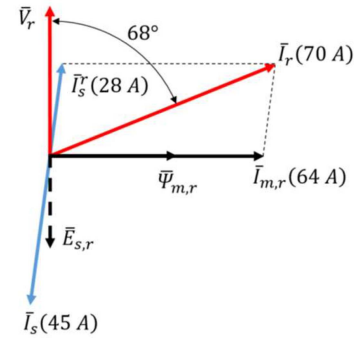


FIGURE 18. Phasors diagram for the fundamental harmonics of currents and voltages according to a single-phase T-equivalent circuit of the motor at steady state.

the machine, the armature current is the minimal one for the produced torque.

In fact, the stator current \bar{I}_s is almost in quadrature to the magnetization current $\bar{I}_{m,r}$ contributing to the average torque generation essentially and not counteracting the main flux $\bar{\Psi}_{m,r}$ at all. On the contrary, if the same magnetizing flux was provided from the armature side at the same torque, the armature current would be ca. 2.5 times larger than its actual value. Hence, the proposed asynchronous starting strategy proves to be effective in keeping the ripple torque at its minimal reluctance component for a given average torque.

For the rotor acceleration, as shown in Fig. 14, the rotor currents amplitudes of Fig. 15 assume roughly 70% of the nominal rotor dc current (100 A). By increasing the rotor currents' amplitudes up to 100% of the nominal rotor current, the EM torque would reach 132 N·m, which amounts to ca. 43% of the synchronous nominal torque. It must be observed there that the armature current would be only 53% of the nominal current and that the RMS rotor current would be ca. 71% of the dc nominal one. That means that neither the armature nor the rotor of the SM would even reach the thermal

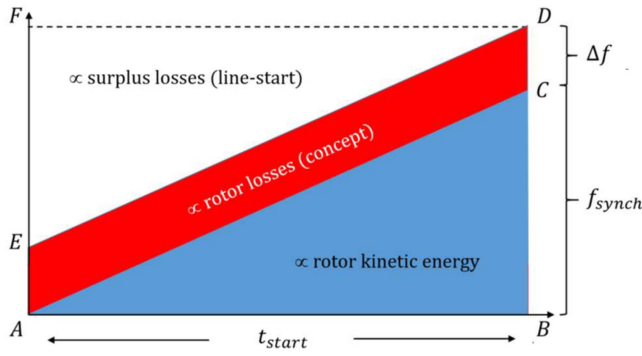


FIGURE 19. Partition of the airgap power.

stress of the nominal behavior. In that condition, the proposed asynchronous start is capable of speeding up the unloaded rotor in

$$t_{\text{run}} = \frac{1}{0.43} 2H = 4.65 H. \quad (51)$$

As a term of comparison, in an exemplar traditional unloaded line start of an SPWFSM with interposition of a reactor [34], where the inrush current is 0.93 p.u. and the supply voltage is 0.22 p.u., the run-up time is increased up to

$$t_{\text{run}} \cong 32 H. \quad (52)$$

In spite of the current- and voltage-limiting measures taken there, which reduce the accelerating torque to 6% of the nominal synchronous one, the rotor reaches the remarkable spot temperature of 198 °C [34].

The suggested starting technique has the advantage of a “constant volt-over-hertz” driving technique, where the drastic reduction of the joule losses, in comparison with the asynchronous line start, is achieved by keeping the airgap power as close as possible to the mechanical one. Fig. 19 allows to estimate the ratio between the kinetic energy stored in the rotor and the total work done by the airgap power during the run-up.

It amounts to circa 83.2% when the excitation frequency ramps up from 2.5 to 27.5 Hz within 9.7 s (Area ABC/Area ABDE). The same efficiency would be only 45.5% over the same time (Area ABC/Area ABDF), in the case of a traditional asynchronous line start at constant frequency with the same accelerating torque. This is enough to conclude that a traditional start would release three times as much heat into the electrical machine as the technique suggested in this article. Moreover, the traditional start wastes the heat into the rotor, which is usually an internal part of the SM and is more difficult to get cooled. On the contrary, the proposed technique releases the heat in the armature essentially, which is already provided with ventilations’ ducts and well-exposed winding heads for cooling purpose.

The machine power factor during the asynchronous start is penalized by the large amount of reactive power needed for the machine magnetization, especially when the SPWFSM has a large airgap or equivalently a large short-circuit ratio.

The presence of an inverter (see Fig. 11) can be then of advantage for the containment of the grid voltage disturbance since the power electronics (PE) itself provides the needed reactive power. This fact reduces the inverter efficiency during the startup, but it does not affect the overall efficiency of the ES significantly, being the starting time a negligible fraction of the entire machine service over a year.

If a power inverter is available for supplying the SM from the armature side, a synchronous start would be more recommendable than an asynchronous one. However, it cannot be ignored that a PE placed between the SM and the grid must have voltage and current ratings comparable with those of the driven SM. Therefore, its remarkable costs could only be justified in the presence of particular driving needs. The suggested alternative starting technique instead cannot provide the entire machine’s nominal torque. So, its use must be envisaged starting at a reduced load, which naturally downsizes the rated power of the needed PE. The starting of a gas turbine-driven generator for instance would be an ideal potential application for the presented technique. The needed firing speed for the compressor, usually 50%÷60% of the nominal speed, scales down the mechanical power for the turbine ignition between 13% and 22% of the generator rated power. Furthermore, the reduced ripple of the torque would be an additional plus considering that the turbine and the synchronous generator are often coupled through a highly efficient but vibration-sensitive gearbox.

Another potential application of this technology could be the auxiliary torque generation for those SAM or wound field LSSM, which have a low LRT and PUT. In other words, where the line-start asynchronous torque at high slip is not large enough for overcoming the load, the proposed starting strategy could provide enough torque for accelerating the rotor up to a certain speed, where the traditional line-start technique can take over that could primarily solve a stall problem and milder both current inrush and rotor thermal stress at the same time.

Another advantage of the spoken technique is the current limitation in the case of rotor blockade for failure or load excess. The current control through the inverter prevents the risk of rotor/armature overheating, with no need for SPUs or SSUs installation. The most evident drawback in comparison with the line-start solutions is the presence of the PE essentially, even though the line start itself requires sometimes special rotor designs or the adoption of current/voltage-limiting additional devices. However, it must be observed that the PE integrates and potentially expands the already needed ES of an SPWFSM. In fact, the proposed multiphase winding together with the inverter could provide additional features besides the traditional ones, which would make the investment in the PE more profitable. They are namely the power system stabilization [35] and the compensation of magnetic and mechanical imbalances [36] via the split rotor technology.

On one side, if the investment for the additional PE would suggest the usage of the presented technology on large

SPWFSM only, on the other side, the condition

$$R_s \gg s\omega_e L_s \quad (53)$$

at standstill ($s = 1$) could be more difficult to be fulfilled with large-size motors. In fact, a larger armature stray inductance together with a lower armature resistance would set the needed excitation frequency so low to pose in the end a technical challenge for its control. The introduction of additional external armature resistors would solve the problem of course. However, the connections between Fig. 7 and their management would be more complicated and relevant in cost.

Finally, the proposed technique, at the state-of-the-art, makes use of slip rings and rotor position sensing device, the removal of which opens a new perspective regarding the future work on this topic.

VI. CONCLUSION

An alternative asynchronous run-up strategy and technology have been presented, which prove to be effective in reducing both the rotor thermal stress and the torsional vibrations, which are present in a traditional asynchronous line start of an SPWFSM. The theoretical foundations of the proposed solution have been disclosed and validated through an experiment and an FEM transient simulation of a partial run-up in a 60 kVA, 50 Hz, four poles SPWFSM. The achieved results have been assessed and discussed by highlighting the pros and cons of the suggested application. When applied to very large SMs, the same strategy could require the usage of external armature resistors so that the minimal excitation frequency does not become too low for being technically controlled. Therefore, the proposed application can best fit, where a medium-power synchronous machine application is essential, but its starting process presents critical aspects in terms of thermal stress and/or torsional vibrations. In that case, the additional benefits deriving from the presented technology, in terms of availability of good PUT level, limitation of the current inrush and more flexible ES performances could help to mitigate and justify the higher costs for the needed PE and sensors.

Additional material: The following supporting information can be downloaded at: <https://doi.org/10.5281/zenodo.8220558>, (Accessed: August 7, 2023), Video: SPWFSM-rotor fed asynchronous start.mp4.

ACKNOWLEDGMENT

The research presented was carried out as a part of “Swedish Hydropower Centre – SVC.” SVC has been established by the Swedish Energy Agency, Elforsk, and Svenska Kraftnät together with Luleå University of Technology, KTH Royal Institute of Technology, Chalmers University of Technology, and Uppsala University (“www.energiforsk.se/program/svenskt-vattenkraft-centrum-2018-2022”).

REFERENCES

- [1] S.-M. Lu, “A review of high-efficiency motors: Specification, policy, and technology,” *Renewable Sustain. Energy Rev.*, vol. 59, pp. 1–12, 2016, doi: [10.1016/j.rser.2015.12.360](https://doi.org/10.1016/j.rser.2015.12.360).
- [2] H. Gavrilă, V. Manescu, G. Paltanea, G. Scutaru, and I. Peter, “New trends in energy efficient electrical machines,” *Procedia Eng.*, vol. 181, pp. 568–574, 2017, doi: [10.1016/j.proeng.2017.02.435](https://doi.org/10.1016/j.proeng.2017.02.435).
- [3] A. T. de Almeida, F. J. T. E. Ferreira, and G. Baoming, “Beyond induction motors—Technology trends to move up efficiency,” *IEEE Trans. Ind. Appl.*, vol. 50, no. 3, pp. 2103–2114, May/Jun. 2014, doi: [10.1109/TIA.2013.2288425](https://doi.org/10.1109/TIA.2013.2288425).
- [4] H. Zhou, G. Liu, J. Zhang, X. Wen, and J. Luo, “Optimal system efficiency and fault-tolerant control of AFPM machines drive for electric bus propulsion,” in *Proc. IEEE Veh. Power Propul. Conf.*, 2013, pp. 1–4, doi: [10.1109/VPPC.2013.6671696](https://doi.org/10.1109/VPPC.2013.6671696).
- [5] H. El Hadraoui, M. Zegrari, A. Chebak, O. Laayati, and N. Guennouni, “A multi-criteria analysis and design of electric motors for electric vehicles,” *World Electr. Veh. J.*, vol. 13, no. 4, 2022, Art. no. 65, doi: [10.3390/wevj13040065](https://doi.org/10.3390/wevj13040065).
- [6] M. Ak, E. Kentel, and S. Savaseneril, “Quantifying the revenue gain of operating a cascade hydropower plant system as a pumped-storage hydropower system,” *Renewable Energy*, vol. 139, pp. 739–752, Feb. 2019, doi: [10.1016/j.renene.2019.02.118](https://doi.org/10.1016/j.renene.2019.02.118).
- [7] T. Holzer and A. Muetze, “Full-size converter operation of hydro power generators: A state-of-the-art review of motivations, solutions, and design implications,” *Elektrotechnik Und Informationstechnik*, vol. 136, no. 2, pp. 209–215, Feb. 2019, doi: [10.1007/s00502-019-0710-3](https://doi.org/10.1007/s00502-019-0710-3).
- [8] J. Koutnik, M. Bruns, L. Meier, and C. Nicolet, “Pumped storage-grid requirements behaviour of large motor-generators and confirmation of compliance through simulation,” in *Proc. HydroVision Int.*, 2011, pp. 19–22.
- [9] M. Valavi and A. Nysveen, “Variable-speed operation of hydropower plants: A look at the past, present, and future,” *IEEE Ind. Appl. Mag.*, vol. 24, no. 5, pp. 18–27, Sep./Oct. 2018, doi: [10.1109/MIAS.2017.2740467](https://doi.org/10.1109/MIAS.2017.2740467).
- [10] J. Antonino-Daviu et al., “Electrical monitoring of damper bar condition in salient pole synchronous motors without motor disassembly,” in *Proc. IEEE 12th Int. Symp. Diagnostics Elect. Mach., Power Electron. Drives*, 2019, pp. 62–68, doi: [10.1109/DEMPED.2019.8864860](https://doi.org/10.1109/DEMPED.2019.8864860).
- [11] T. Glinka and J. Bernatt, “Asynchronous slip-ring motor synchronized with permanent magnets,” *Arch. Elect. Eng.*, vol. 66, no. 1, pp. 199–206, 2017, doi: [10.1515/ae-2017-0015](https://doi.org/10.1515/ae-2017-0015).
- [12] D. Mingardi, N. Bianchi, and M. D. Pre, “Geometry of line start synchronous motors suitable for various pole combinations,” *IEEE Trans. Ind. Appl.*, vol. 53, no. 5, pp. 4360–4367, Sep./Oct. 2017, doi: [10.1109/TIA.2017.2702581](https://doi.org/10.1109/TIA.2017.2702581).
- [13] B. Zöhra, M. Akar, and M. Eker, “Design of a novel line start synchronous motor rotor,” *Electron. (Basel)*, vol. 8, no. 1, 2018, Art. no. 25, doi: [10.3390/electronics8010025](https://doi.org/10.3390/electronics8010025).
- [14] B. Yan, Y. Yang, and X. Wang, “Design of a large capacity line-start permanent magnet synchronous motor equipped with hybrid salient rotor,” *IEEE Trans. Ind. Electron.*, vol. 68, no. 8, pp. 6662–6671, Aug. 2021, doi: [10.1109/TIE.2020.3008360](https://doi.org/10.1109/TIE.2020.3008360).
- [15] W. Lyskawinski, “Comparative analysis of energy performance of squirrel cage induction motor, line-start synchronous reluctance and permanent magnet motors employing the same stator design,” *Arch. Elect. Eng.*, vol. 69, no. 4, pp. 967–981, 2020, doi: [10.24425/ae.2020.134642](https://doi.org/10.24425/ae.2020.134642).
- [16] V. J. Sarac and G. Stefanov, “Various rotor topologies of line-start synchronous motor for efficiency improvement,” *Power Electron. Drives*, vol. 5, no. 1, pp. 83–95, 2020, doi: [10.2478/pead-2020-0006](https://doi.org/10.2478/pead-2020-0006).
- [17] J. Bredthauer and N. Struck, “Starting of large medium voltage motors: Design, protection, and safety aspects,” *IEEE Trans. Ind. Appl.*, vol. 31, no. 5, pp. 1167–1176, Sep./Oct. 1995, doi: [10.1109/28.464534](https://doi.org/10.1109/28.464534).
- [18] M. Centner, T. Getschmann, M. Chisholm, S. A. Smith, and M. Melnick, “Run-up protection in high-inertia synchronous motor applications,” *IEEE Trans. Ind. Appl.*, vol. 58, no. 4, pp. 4261–4270, Jul./Aug. 2022, doi: [10.1109/TIA.2022.3167991](https://doi.org/10.1109/TIA.2022.3167991).

- [19] E. L. Owen, "Torsional coordination of high speed synchronous motors—Part I," *IEEE Trans. Ind. Appl.*, vol. IA-17, no. 6, pp. 567–571, Nov. 1981, doi: [10.1109/TIA.1981.4504006](https://doi.org/10.1109/TIA.1981.4504006).
- [20] J. O. Ojo, V. Ostovic, T. A. Lipo, and J. C. White, "Measurement and computation of starting torque pulsations of salient pole synchronous motors," *IEEE Trans. Energy Convers.*, vol. 5, no. 1, pp. 176–182, Mar. 1990, doi: [10.1109/60.50829](https://doi.org/10.1109/60.50829).
- [21] M. Popescu, T. J. E. Miller, M. I. McGilp, F. J. H. Kalluf, C. A. da Silva, and L. von Dokonal, "Effect of winding harmonics on the asynchronous torque of a single-phase line-start permanent-magnet motor," *IEEE Trans. Ind. Appl.*, vol. 42, no. 4, pp. 1014–1023, Jul./Aug. 2006, doi: [10.1109/TIA.2006.876078](https://doi.org/10.1109/TIA.2006.876078).
- [22] M. Aoyama, T. Mizuta, and K. Ito, "Verification of effect of secondary conductor bar on starting characteristics in line-start type self-excited wound-field synchronous motor," *IET Electr. Power Appl.*, vol. 14, pp. 2818–2831, Feb. 2021, doi: [10.1049/iet-epa.2020.0497](https://doi.org/10.1049/iet-epa.2020.0497).
- [23] *IEEE Guide for Evaluation of Torque Pulsations During Starting of Synchronous Motors*, IEEE Standard 1255-2000, 2000, doi: [10.1109/IEEESTD.2000.91941](https://doi.org/10.1109/IEEESTD.2000.91941).
- [24] A. M. Zyuzev, V. P. Metel'nikov, and D. P. Stepanyuk, "Control of startup of an asynchronous thyristor electric drive taking into account a limited heating and network influence," *Russian Elect. Eng.*, vol. 83, no. 9, pp. 504–507, 2012, doi: [10.3103/S106837121209012X](https://doi.org/10.3103/S106837121209012X).
- [25] K. N. Lebedev, G. V. Lebedeva, and N. N. Gracheva, "Technical and economic aspects of the use of soft starters for asynchronous electric drives," *IOP Conf. Ser., Earth Environ. Sci.*, vol. 659, no. 1, 2021, Art. no. 012027, doi: [10.1088/1755-1315/659/1/012027](https://doi.org/10.1088/1755-1315/659/1/012027).
- [26] I. Y. Braslavskii, A. V. Kostylev, and D. P. Stepanyuk, "Estimate of the influence of smooth-start regimes of asynchronous motors on losses and supply mains," *Russian Elect. Eng.*, vol. 80, no. 9, pp. 506–510, 2009, doi: [10.3103/S1068371209090089](https://doi.org/10.3103/S1068371209090089).
- [27] G. Pellegrino, T. M. Jahns, N. Bianchi, W. Soong, and F. Cupertino, *The Rediscovery of Synchronous Reluctance and Ferrite Permanent Magnet Motors*. Cham, Switzerland: Springer, 2016, doi: [10.1007/978-3-319-32202-5](https://doi.org/10.1007/978-3-319-32202-5).
- [28] A. E. Fitzgerald, C. Kingsley, and S. D. Umans, *Electric Machinery*, 6th ed. New York, NY, USA: McGraw Hill, 2003.
- [29] A. Ivanov-Smolensky, "Calculation of no-load current," in *Electrical Machines*, 1st ed. Moscow, Russia: Mir Publisher, 1982, ch. 40, sec. 4, pp. 71–72.
- [30] I. M. Caney, "Equivalent circuits of synchronous machines for calculating quantities of the rotor during transient processes and asynchronous starting—Part II: Salient pole machines," *Brown Boveri Rev.*, vol. 3, no. 70, pp. 134–144, Mar. 1970.
- [31] R. Felicetti and U. Lundin, "Salient pole electrical machine," Swedish Patent SE 545 283, Jun. 20, 2023.
- [32] S. J. Salon, *Finite Element Analysis of Electrical Machines*. New York, NY, USA: Springer, 1995.
- [33] S. L. Ho and W. N. Fu, "A comprehensive approach to the solution of direct-coupled multislice model of skewed rotor induction motors using time-stepping eddy-current finite element method," *IEEE Trans. Magn.*, vol. 33, no. 3, pp. 2265–2273, May 1997.
- [34] M. Canay, "Asynchronous starting of a 230 MVA synchronous machine in 'Vianden 10' pumped storage station," *Brown Boveri Rev.*, vol. 61, no. 7, pp. 313–318, Jul. 1974.
- [35] A. Nocoń and S. Paszek, "A comprehensive review of power system stabilizers," *Energies*, vol. 16, no. 4, Feb. 2023, Art. no. 1945, doi: [10.3390/en16041945](https://doi.org/10.3390/en16041945).
- [36] J. K. Nøland, S. Nuzzo, A. Tessarolo, and E. F. Alves, "Excitation system technologies for wound-field synchronous machines: Survey of solutions and evolving trends," *IEEE Access*, vol. 7, pp. 109699–109718, 2019.



ROBERTO FELICETTI received the first M.S. degree in electrical engineering from University La Sapienza, Rome, Italy, in 1997, and the second M.S. degree in renewable electricity production and the Ph.D. degree in science of electricity, by defending a thesis about the transient analysis of the asynchronous run-up in salient pole wound field synchronous machines, from Uppsala University, Uppsala, Sweden, in 2018 and 2023, respectively.

From 1999 to 2002, he was an Electrical Machines Designer with Robert Bosch GmbH, Bülhertal, Germany. As a member of the Hydropower Group within Uppsala University, he has taken part in the Hydroflex EU-project (Horizon 2020 programme) from 2018 to 2022. He is currently a Researcher with Uppsala University. His research interests include the design and usage of large electrical machines for improving the efficiency and durability of hydro-power plants.



VINÍCIUS M. DE ALBUQUERQUE received the B.S. and M.Sc. degrees in electrical engineering from the Federal University of Juiz de Fora (UFJF), Juiz de Fora, Brazil, in 2017 and 2020, respectively. He is currently working toward the Ph.D. degree in special focus on generator design for efficient energy harvesting with Uppsala University, Uppsala, Sweden.

During both degrees, he acted as Undergraduate (from 2013 to 2017) and Graduate (from 2018 to 2019) Researcher with Modern Lighting Research Group (NIMO), Engineering School, UFJF. He was a beneficiary of the Brazilian Program Science Without Borders, completing two semesters with the University of Minnesota, Minneapolis, MN, USA, from 2015 to 2016. His current research interests include electronic energy conversion, hydropower, hydro-oscillating power conversion, and the modeling and control of electronic power converters for grid connection and permanent magnet synchronous machines.



URBAN LUNDIN received the Ph.D. degree in condensed matter theory from Uppsala University, Uppsala, Sweden, in 2000.

From 2001 to 2004, he was a Postdoctor with the University of Queensland, Brisbane, Australia. In 2004, he joined the Division for Electricity, Uppsala University. He is currently a Professor of electricity with a specialization in hydropower systems. His research focuses on synchronous generators and their interaction with mechanical components and the power system. He leads the Hydropower Group and has been involved in the industrial implementation of research projects. Current research interests concern excitation systems for magnetic balancing, magnetic bearings, and synthetic inertia. He is currently a Professor in Electrical Engineering with specialization in Hydro-power at Uppsala University, Sweden.